Automated Road Information Extraction From Mobile Laser Scanning Data

Haiyan Guan, Jonathan Li, *Senior Member, IEEE*, Yongtao Yu, Michael Chapman, and Cheng Wang, *Member, IEEE*

***Abstract*—This paper presents a survey of literature about road feature extraction, giving a detailed description of a Mobile Laser Scanning (MLS) system (RIEGL VMX-450) for transportation-related applications. This paper describes the development of automated algorithms for extracting road features (road surfaces, road markings, and pavement cracks) from MLS point cloud data. The proposed road surface extraction algorithm detects road curbs from a set of profiles that are sliced along vehicle trajectory data. Based on segmented road surface points, we create Geo-Referenced Feature (GRF) images and develop two algorithms, respectively, for extracting the following: 1) road markings with high retroreflectivity and 2) cracks containing low contrast with their surroundings, low signal-to-noise ratio, and poor continuity. A comprehensive comparison illustrates satisfactory performance of the proposed algorithms and concludes that MLS is a reliable and cost-effective alternative for rapid road inspection.**

***Index Terms*—Mobile Laser Scanning (MLS), pavement cracks, road markings, road surfaces, traffic safety.**

I. Introduction

ROAD transportation plays a vital role in the lives of people worldwide because it unites people for business or pleasure by connecting small and large cities and urban and rural communities, as well as connecting a country with its neighbors, to enable the safe movement of goods, people, and services. Roads and their features (including bridges, tunnels, road markings, supporting structures, junctions, crossings, and interchanges) are carefully designed and constructed to increase road traffic safety, improve the efficient use of the overall network, and reduce the harm (e.g., deaths, injuries, and property damage) on the overall network from traffic collisions.

To safely keep people on the move, transportation departments or agencies in cities or countries must periodically perform road surveying. The documentation of road infrastructure includes both road surface geometry (e.g., longitudinal and transverse slopes, lane width, and number of lanes) and road environment (e.g., road markings, cracks, street signs, trees, vegetation, and traffic light poles). The surveyed data are used not only for transportation department administrations to maintain, rehabilitate, and reconstruct current traffic and parking infrastructure but also to assess policies and practices affecting roadways.

However, these transportation-related road features are manually collected by involving an engineer annotating a digital map or a manual classification of spatially referenced video images. The operations for inspecting road features of large-scale road networks are time consuming, labor intensive, and costly. Mobile mapping refers to a means of collecting geospatial data using sensors mounted on a mobile platform. The development of a mobile mapping system was primarily driven by advances in digital imaging and direct georeferencing technologies. Image-based mobile mapping systems greatly impact conventional transportation surveying and mapping [1]. The technology of 3-D laser scanning has further fuelled model-based road design and automated machine guidance.

A vehicle-borne Mobile Laser Scanning (MLS) system, which uses a laser beam to scan a visible surface and record the beam traveling time and the reflected energy from the surface to obtain its geometry and intensity data in the form of 3-D point clouds, has been used in transportation agencies for a broad spectrum of applications, such as route planning and preliminary highway design [2]. Compared with photogrammetry and field surveys, an MLS system captures high point density and accurate 3-D point clouds in a relatively short time period [3], [4]. However, an MLS system, consisting of a Global Navigation Satellite System/Initial Measurement Unit (GNSS/IMU) integration system, laser scanners, and several high-resolution cameras with a computer control device, is still in its infancy and has only been commercially available for several years [5]. Thus, there is an urgent need to investigate MLS as a reliable and cost-effective alternative for road inspection, particularly in regard to effective road traffic safety.

In this paper, we develop three algorithms for extracting road features (including road surfaces, road markings, and pavement cracks), which are the main factors for road traffic safety. For example, asphalt concrete-surfaced pavement distress measurement is an indispensable part of pavement management systems to cost effectively maintain and rehabilitate roads. Cracking, which is caused by fracture due to excessive loading, fatigue, thermal changes, moisture damage, slippage, or contraction, is the most common type of asphalt concrete-surfaced pavement

Manuscript received December 2, 2013; revised March 3, 2014 and April 23, 2014; accepted May 29, 2014. Date of publication July 8, 2014; date of current version January 30, 2015. This work was supported by a discovery grant from the Natural Sciences and Engineering Research Council of Canada that was awarded to J. Li. The Associate Editor for this paper was H. Huang.

H. Guan is with the Department of Geography and Environmental Management, University of Waterloo, Waterloo, ON N2L 3G1, Canada (e-mail: h6guan@uwaterloo.ca).

J. Li is with the Ministry of Education Key Laboratory of Underwater Acoustic Communication and Marine Information Technology, Xiamen University, Xiamen 361005, China, and also with the Department of Geography and Environmental Management, University of Waterloo, Waterloo, ON N2L 3G1, Canada (e-mail: junli@xmu.edu.cn).

Y. Yu and C. Wang are with the Department of Computer Science, Xiamen University, Xiamen 361005, China (e-mail: allennessy.yu@gmail.com; cwang@xmu.edu.cn).

M. Chapman is with the Department of Civil Engineering, Ryerson University, Toronto, ON M5B 2K3, Canada (e-mail: mchapman@ryerson.ca).

Color versions of one or more of the figures in this paper are available online at http://ieeexplore.ieee.org.

Digital Object Identifier 10.1109/TITS.2014.2328589

distress [6], [7]. Road markings on paved roadways, a critical type of road feature in traffic management systems, have important functions in providing guidance and information to drivers and pedestrians. Along with pavement condition and road topography, the lack of visibility of road markings is a key element in road accidents where the road itself is the cause. Particularly, in highly populated urban environments, high accident rates are caused by the absence of clearly presented road signals [8]. As a result, with the developed algorithms, a practical system that monitors road environments is needed to maintain high technical standards for road traffic safety.

II. Related Work

Emerging in 2003, MLS has attracted much attention for mainly transportation-related surveys [9], [10]. The development of MLS has created a data revolution. Using an MLS system, a mobile mapping crew can drive on a highway, rural road, railroad, or the shoreline of a river or a lake. Along the way, the system captures trees, bridges, streetlights, buildings, power lines, other small street-scene objects (e.g., cracks and road markings), and virtually anything visible to the eyes in three dimension. The collected data represent a totally immersive 3-D view of objects and surroundings. In the following sections, a variety of methods developed for extracting roads, road markings, and cracks from MLS data are reviewed.

A. Studies on Road Surface Extraction

Although much effort has been made to extract road features from MLS data, efficient interpretation methods are still in a state of early development. Most algorithms roughly follow these common steps when interpreting MLS point clouds: 1) detection of planar or smooth surfaces and 2) classification of points or point clusters using data features, such as local point patterns, intensity, and pulse return information [11]. In the first category, some model fitting methods, such as Hough transform [12], RANdom SAmple Consensus (RANSAC) [13], and weighted least square linear fitting [14], were widely employed to directly identify road surfaces. In the second category, because point density drops perpendicular to the line of travel, it was used to separate road surfaces [15], [16]. However, these methods may fail when erroneous points exist in MLS data. Recently, intensity has become another factor considered in road feature detection [17].

Apart from MLS data characteristics, road properties have been explored to facilitate road feature extraction. For example, because road curbs represent road boundaries in most urban environments, some researchers detected curbs to identify road regions and to calculate obstacle-free areas [18], [19]. Reference [20] combined prior knowledge about the minimal width of roads and elevation information for classifying road regions and edges. To compensate for the limitations of MLS data, some researchers integrated MLS data with other data sources, such as video cameras [21] and Airborne Laser Scanning data [22].

Most of these reviewed methods, which are based on mathematical estimations, could be time consuming and computationally intensive for such large volumes of MLS data. Little research has been carried out to extract road surfaces based on trajectory data, which precisely record real-time position information of the vehicle. In addition, most urban roads are designed with curbs for separating them from pedestrian sidewalks. There is a need to develop a road surface extraction algorithm to accurately estimate road edges based on road features and MLS data characteristics.

B. Studies on Pavement Crack Extraction

Currently, visual measurement techniques have been mostly explored to inspect and evaluate pavements in videos or digital images collected from a specially equipped vehicle. Reference [7] summarized the following six common segmentation and classification methods: regression/relaxation thresholding, Canny edge detection, crack seed verification, multiscale wavelets, iterative clipping method, and dynamic optimization-based method. Reference [23] also demonstrated that F^* seed growing, a dynamic optimization-based method, can effectively handle blurry and discontinuous pavement images. However, most algorithms are computationally intensive. Based on either grayscale discontinuity or similarity, the effectiveness of thresholding-based segmentation methods mostly depends on pavement environments and materials, leading to unreliable crack detection results [24], [25]. Wavelet-based transforms, such as beamlet, contourlet, and their variants, are another common type of technique for crack extraction [26]. However, due to the anisotropic properties of wavelets, they often fail to process cracks with high curvature or poor continuity.

Mathematical-morphology-based methods have been used to extract cracks in pavement images [27]. However, these algorithms are limited to three structural elements (disk, line, and square) and by the choice of parameters. Much effort on crack extraction has been made in the fields of artificial intelligence, data mining, machine learning, and neural networks [28], [29]. However, the selection of parameters depends on crack variations and image quality. Additionally, image-/video-based crack extraction algorithms suffer from the influence of several environmental factors, such as the following: 1) shadows cast by trees and moving vehicles; 2) weather conditions; and 3) the imaging time of day, which has the greatest impact on the visibility of road surfaces.

C. Studies on Road Marking Extraction

When it comes to road marking extraction from either digital photographs or videos [30]–[34], precise geometrical information is limited by the previously mentioned three environmental factors. Thus, although work on road marking extraction from either digital photographs or videos has been pursued for years, fully automated road marking extraction has remained a challenge.

The MLS data indicate that road markings painted on road surfaces are highly retroreflective; thus, high reflectance in the form of intensity has been widely used to extract road markings [10], [13], [35]–[37]. Reference [35] outlined road markings by first applying an interpolation method to MLS points, segmenting Geo-Referenced Feature (GRF) images based on intensity and elevation information, and extracting road markings by integrating their semantic knowledge (e.g., shape and size).

Fig. 1. RIEGL VMX-450 system with an inset picture of the laser scanners, cameras, and the navigation system mounted on the roof rack.

However, intensity data are highly dependent on the following: 1) the scanning range from the laser sensor to the target; 2) the incidence angle of the laser beam; and 3) material properties of the target. Thus, prior to segmentation, intensity data must be normalized. Jaakkola *et al.* [36] applied radiometric correction to MLS intensity data. Vosselman [37] introduced a distance-dependent intensity normalization method, by which several types of road markings are identified. However, the extracted markings are incomplete and contain distinguishable noise. The predefined shapes used for fitting to road marking segments are considered the cause. As most algorithms applied a globally threshold-based segmentation to intensity data, much noise is introduced, resulting in a less effective extraction of road markings.

III. MLS System and MLS Data

A. RIEGL VMX-450 System

A RIEGL VMX-450 system used in this study is composed of the following: 1) two RIEGL VQ450 laser scanners; 2) four charge-coupled device cameras; and 3) a set of Applanix POS LV 520 processing systems containing two GNSS antennas, an IMU system, and a distance measurement indicator. As shown in Fig. 1, by using a point-of-sale computer system, the previously mentioned components are integrated, fixed within a case, and mounted on the roof of a vehicle. The accuracy of the resultant positions and orientations largely determines the overall performance of the RIEGL VMX-450 system.

The navigation solution in the RIEGL VMX-450 system uses two dual-frequency GNSS antennas, which are referred to as a primary receiver and a secondary receiver. Both receivers provide raw GNSS satellite observable information to a POS LV computer system. The secondary receiver is used by a GPS Azimuth Measurement System (GAMS) to aid heading. Its data are used in conjunction with information from the primary receiver for GAMS heading calculations.

In Fig. 1, two laser scanners are symmetrically configured on the left and right sides, pointing toward the rear of the vehicle at an angular heading of approximately 135°. This configuration is called a "butterfly" configuration pattern. The full specifications for laser scanners can be found on the RIEGL website. Note that the field of view of a scanner is 360°, which is also termed as "full circle" owing to a motorized mirror scanning mechanism. Thus, the scanned data of the two scanners form a slant gridlike pattern. The scanning data are complemented by the images from a camera system. According to pulse per second from the primary GNSS receiver, the scanned data and digital images are synchronized with positions and orientations by POS LV 520 system.

TABLE I
Parameters of the Geo-Referenced Equation

Parameters	Description
r_p^m	Position vector of GPS antenna in the mapping coordinate system.
$r_{GPS}^m(t)$	Position vector of GPS antenna in the mapping coordinate system.
r_p^S	Relative position vector of point P in the laser scanner coordinate system.
$r_{IMU/S}^{IMU}$	Lever arm offset from the IMU origin to the laser scanner.
$r_{IMU/GPS}^{IMU}$	Lever arm offset from the IMU origin to the GNSS antenna.
$R_{IMU}^m(t)$	Rotation matrix between the IMU and mapping coordinate systems.
R_S^{IMU}	Rotation matrix between the laser scanner and IMU coordinate systems.

B. Georeferencing and Scanning Parameters

Calculation of ground coordinates for illuminated objects, which is termed as "georeferencing," from an MLS system can be found in [38]. The laser scanner is georeferenced when its position and orientation relative to the mapping coordinate system are known by a set of navigation systems. These data must be precisely time stamped for sensor integration and determination of the exact coordinates of mapping points [39]. The coordinates of a target P can be calculated by

$$r_p^m = r_{\mathrm{GPS}}^m(t) + R_{\mathrm{IMU}}^m(t)\left(r_{\mathrm{IMU}/S}^{\mathrm{IMU}} - r_{\mathrm{IMU/GPS}}^{\mathrm{IMU}} + R_S^{\mathrm{IMU}} r_p^S\right) \quad (1)$$

where the parameters and their descriptions are listed in Table I.

Equation (1) defines the relationship among all observation parameters for producing georeferenced point clouds. To examine final point accuracy, we discuss typical errors in these observations.

1) *IMU attitude errors:* The IMU component consists of three orthogonal accelerometers and three orthogonal gyroscopes. Accordingly, systematic sensor errors include accelerometer biases and gyro drifts. Typically, as the IMU components are supplied by two or three different system manufacturers, their accuracies can be examined from the manufacturers' technical specifications.
2) *Positioning errors*: The positioning accuracy of the GNSS subsystem is influenced by the following factors: multipath, atmospheric errors, baseline length, poor satellite geometry, and loss of lock. Therefore, the absolute level of the positioning accuracy for an MLS survey is difficult to quantify.
3) *Laser scanner errors*: Most laser producers provide two main error components: errors in distance and errors in angles. Distance error is caused by the internal accuracy of the clock because the internal clock measures the time of flight and the width of the output laser pulse; angle error is due to the angular resolution of the laser scanner angle encoder and the uncertainty of beam divergence.
4) *Boresight errors*: The boresight errors result from the misalignments between IMU and laser scanner measurement axes. To process laser scanning data, the location

TABLE II
SCANNING PARAMETERS

Symbol	Quantity
S_s	Scan speed/scan rate
S_G	Vehicle speed
L_{Dist}	Scan-line-to-scan-line spacing
P_{Dist}	Point-to-point spacing
T_{Dist}	Target distance
$L_{Increment}$	Scan line incremental
$P_{Density}$	Average point density

of the scanner and its orientation in relation to IMU must be precisely known because alignment errors will be propagated over the distance between the sensor and the object being scanned.

5) *Lever arm offset errors*: Usually, the origins of laser scanners and IMU cannot be collocated; thus, the lever arm offsets must be known in order to accurately obtain georeferenced MLS point clouds.

The preceding discussion of error sources for an MLS system demonstrates that the accuracy of MLS point clouds depends on the underlying accuracy of the GNSS/IMU navigation solution and laser scanners. Among these errors, two possible error sources (boresight and lever arm) can be recovered by system calibration. In fact, the overall accuracy of MLS point clouds is mainly affected by the navigation solution because the multipath effects and signal shading (caused by high-rise buildings and trees along the street) deteriorate the GNSS conditions in a moving vehicle [3]. GNSS positioning errors in MLS systems have a great impact on the overall error budget, owing to a short distance (even about several to 10 m) between a laser scanner and a scanned object. To improve MLS data accuracy, geometric correction is indispensable.

For a laser scanner, the following scanning parameters are defined:

$$S_s\,[\text{line/s}] = L_{\text{Increment}}[\text{deg}] \times \text{PRR}[Hz]/360^\circ \quad (2)$$

$$L_{\text{Dist}}\,[\text{m/line}] = S_G\,[\text{m/s}]\,/S_s\,[\text{line/s}] \quad (3)$$

$$P_{\text{Dist}}[m] = \tan\left(L_{\text{Increment}}[\text{deg}]\right) \times T_{\text{Dist}}[m] \quad (4)$$

$$P_{\text{Density}}\left[\text{pt/m}^2\right] = 1/\left(P_{\text{Dist}}[m] \times L_{\text{Dist}}[m]\right) \quad (5)$$

where the parameters and their descriptions are listed in Table II.

From (2)–(5), an average point density of the collected data depends on scan speed S_s, vehicle speed S_G, and system effective measurement rate or *pulse repetition* rate (PRR). Scan speed S_s is determined by PRR and scan line incremental. Scan-line-to-scan-line spacing L_{Dist} is proportional to S_G and inversely proportional to S_s, indicating that the higher the vehicle speed, the lower the scan-line-to-scan-line spacing in the running direction, whereas the higher the scan speed, the higher the scan-line-to-scan-line spacing. However, point-to-point spacing P_{Dist} in a single scan line varies significantly with scan angles and scan counts but very little with vehicle speeds. The point density within scan lines varies greatly with both the vertical orientation of the features being scanned and the distance from the scanner [40].

C. Study Areas and MLS Data

The survey area is within Xiamen Island (longitude 118° 04′ 04″ E, latitude 24° 26′ 46″ N), a part of the City of Xiamen, a major city on the southeast coast of China. In addition to Xiamen Island, Xiamen City includes Gulang Islet and part of the rugged mainland coastal region from the left bank of the Jiulong River in the west to the islands of Xiang'an in the northeast. The surveyed Huandao Road, which is called a golden costal line, is a busy seaside green corridor for tourism, sightseeing, leisure, and recreation; as a result, moist weather and excessive loading cause a number of cracks spreading along the road. The data were acquired on April 23, 2012, by a RIEGL VMX-450 system.

As discussed in Section III-B, the navigation solution has great impact on the accuracy of the MLS data. In general, at least four satellites in view with position dilution of precision of six or lower are required for the standard positioning service.

To evaluate the overall performance of the collected MLS data, reference data, at least one level more accurate than the system being tested, are collected. In most cases, corner points of objects on the street and white road markings on the road surfaces are selected because they are conveniently identified in point clouds for accuracy assessment. Approximately 30 reference points at the corners of road markings were measured by Leica personnel in Xiamen. With the reference points, the accuracy of the collected MLS data is assessed.

As shown in Table III, the mean standard deviations of planimetric accuracy for the left and right laser scanners are 0.042 and 0.033 m, respectively. The mean standard deviations of vertical accuracy for two laser scanners are 0.017 and 0.021 m, respectively. Notice that the minimum standard deviation appears at the check points measured near the base station with good GPS coverage. In spite of check point errors, the data accuracy is still consistent with the accuracy of the navigation system and even outperforms the Applanix's specification. The errors are lower than ±5 cm and meet the requirements of data accuracy for urban surveying.

During this survey, we predefined two types of parameters: mission parameters and scanner parameters.

Mission Parameters: The mission parameter category includes T_{Dist} and S_G. The surveyed Huandao Road is quite busy, the average driving speed ranges from 30 to 50 km/h. The buildings (e.g., high-rise residential apartments and commercial buildings) are located along this typical urban road. Thus, we kept $T_{\text{Dist}} = 30$ m and $S_G = 30$ km/h.

Scanning Parameters: As for scanning parameters, we used the default values for all parameters, such as scan mode (line), scan line start (0°), scan line end (360°), scan increment angles (0.1143°), and PRR (550 kHz). Thus, according to (2)–(5), at the vehicle speed of 30 km/h, the scan speed, the line distance, the point distance, and the average point density are estimated as 200 line/s, 0.0583 m, 0.0598 m, and 286.44 point/m^2, respectively. Point density, which strongly relies on the incidence angle and the nominal distance to the target, can be determined by dividing the number of MLS points on the plane by the total area.

TABLE III
ACCURACY OF THE COLLECTED MLS DATA

	Mean standard deviation		Minimum standard deviation		Maximum standard deviation	
	Left laser scanner	Right laser scanner	Left laser scanner	Right laser scanner	Left laser scanner	Right laser scanner
Elevation accuracy	0.017	0.021	0.008	0.007	0.019	0.025
Planimetric accuracy	0.042	0.033	0.025	0.023	0.057	0.049

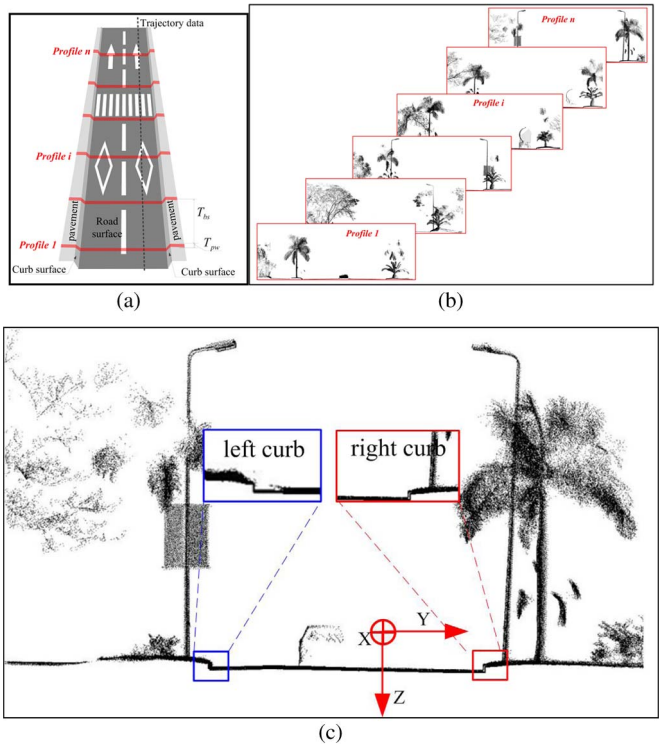

Fig. 2. Illustration of curb-based road surface extraction from MLS data. (a) Trajectory-based MLS data profiling. (b) A number of profile examples. (c) Close-up views of road curbs.

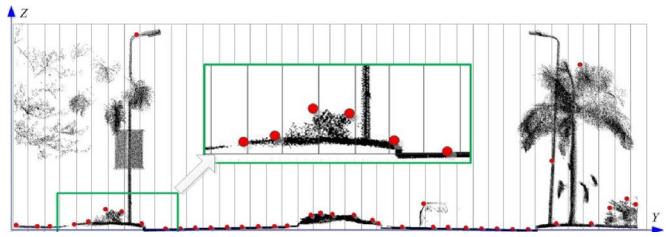

Fig. 3. Illustration of pseudo scan line generation.

IV. ROAD FEATURE EXTRACTION

A. Road Surface Extraction

Note that curbs are road boundaries that separate pedestrian pavements or other green spaces from road surfaces. We propose a curb-based road surface extraction algorithm with the assistance of vehicle trajectory data. As a mobile mapping crew drives along road surfaces, trajectory data are useful for curb detection. The proposed algorithm is composed of four steps: 1) data profiling; 2) pseudo scan line generation; 3) curb detection; and 4) road edge fitting.

Perpendicular to trajectory data, we first partition point clouds into a number of data blocks with a given length (T_{bs}). A profile is sliced for each data block with a given width (T_{pw}). Therefore, each profile contains points pertaining to road surfaces and points pertaining to objects beyond the road such as trees, cars, or curbs. As shown in Fig. 2(a), red rectangles represent profiles. All points for each profile are projected onto the plane perpendicular to the line of travel, as shown in Fig. 2(b). For the MLS system used in this study, the vehicle frame is defined as the right-handed orthogonal coordinate system with its origin at an arbitrary user-defined point. The orientation of the vehicle frame is fixed so that the x-axis is toward the front of the vehicle, the y-axis is toward the right of the vehicle, and the z-axis is toward the bottom of the vehicle. Fig. 2(c) shows a profile image by projecting all points within the profile onto the YoZ-plane in the vehicle frame. A close-up view demonstrates that curbs, vertical or nearly vertical to road surfaces, are sharp height jumps; therefore, we estimate curbs by slope and elevation difference criteria and, finally, separate road points from nonroad points.

To this end, each profile is vertically divided into a number of bars with a bar size of T_{cs}. The bar size depends on the point density of MLS data within experiments. Second, a sampling strategy is carried out for each bar to select a principal point, as shown in Fig. 3. To determine the principal point within a bar, a Quick Sort algorithm is used to sort all the points within the bar in elevation. Next, from the lowest point, we calculate the elevation differences ΔL_j $(j = 1, 2, 3, \ldots, N)$ of two consecutive points and group them into different layers. N is the number of the points in a bar. The two consecutive points are labeled into the same layer if and only if the elevation difference lies below a predefined threshold, that is, $\Delta L_j < L_T$. Otherwise, a new layer is created to separate the two points. Usually, we keep $L_T = 5$ cm. Based on the assumption that points belonging to road surface are within the lowest layer, principal points within each bar are determined by selecting the point with the highest elevation within the lowest layer. With this scheme, most outliers, such as tree points, over the road are removed. The extracted points are then reorganized into a pseudo scan line, which maintains road surface points and critical road features with less disruptive noise.

The proposed algorithm for detecting curbs is, based on both slope and elevation evaluation, implemented at the scanning center in two opposing ways. We mathematically define the slope between two consecutive points in a generated pseudo scan line and the elevation difference of a point relative to its neighborhood in the pseudo scan line. Assume that slopes at the borders of pavements and roadways are usually larger than that of continuous points on the roadways. Moreover, pavement points have larger elevations than roadway points in a neighborhood. We use two criteria to detect whether a point is a curb. First, the slope criterion is used to detect nonroad points (e.g., car points and curbs). Then, the elevation difference criterion

is used to detect curbs from the nonroad points. Street design and construction manuals in many countries demonstrate that curb height generally ranges from 10 to 20 cm. We, thus, mathematically define the following two observations as

$$\forall\, p_i : \begin{cases} \text{if } (S_{\text{slope}} > S_T \;\&\; (G_{\min} \le G_i \le G_{\max})) & \text{curb candidate} \\ \text{otherwise,} & \text{noncurb point} \end{cases} \tag{6}$$

where S_{slope} denotes the slope of two consecutive points, S_T is a given slope threshold, and G_i is the elevation difference of a point and its neighbor. $G_{\min}$ and $G_{\max}$ are the minimum and maximum thresholds, respectively. S_{slope} is defined as

$$S_{\text{slope}} = \arctan\left(\frac{Z_{i+1} - Z_i}{\sqrt{(X_{i+1} - X_i)^2 + (Y_{i+1} - Y_i)^2}}\right)$$
$$S_{\text{slope}} \in \left[-\frac{\pi}{2}, \frac{\pi}{2}\right] \tag{7}$$

where (X_i, Y_i, Z_i) and $(X_{i+1}, Y_{i+1}, Z_{i+1})$ are the coordinates of two consecutive points in a pseudo scan.

Note that (7) can take both positive and negative signs. A positive slope means a point sequence entering a nonroad point from the road at the curb boundary, whereas a negative slope represents a point sequence leaving a nonroad point from the road at the curb boundary. In our algorithm, we start the labeling process from the vehicle position on the road surface. In other words, the initial labeling is entering from the road into the curb. Therefore, once a point, p_i gets a slope S_{slope} greater than S_T, it means that the point reaches a possible curb. It will be labeled as a curb candidate. From all the curb candidates, including curbs or some other objects such as cars over the road, we must check their elevations to detect real curbs. If a curb candidate's elevation difference g_i at its vicinity is within the range of $[G_{\min}, G_{\max}]$, the curb candidate is labeled as a curb; otherwise, it will be labeled as a noncurb point. As the survey vehicle moves along the road surface, with prior knowledge of the road, we select curb candidates closest to the scanning center as curbs.

All curbs detected from profiles are sparse because we section MLS data along vehicle trajectory data into a number of data blocks at a certain length. Therefore, we use a cubic spline interpolation method to generate two smooth road edges from these curb points and, finally, separate road points from nonroad points.

B. Applications of Road Surface Extraction: Road Markings

Based on the extracted road surface points, we propose a road markings recognition framework, which includes the following three steps.

1) GRF image generation, which locally and globally interpolates the extracted road surface points into a GRF image based on elevation and intensity data via an extended inverse distance weighted method. Although interpolation might cause a loss of accuracy, it is computationally efficient to process enormous volumes of MLS data using established image processing algorithms.
2) Point-density-dependent thresholding, which adaptively segments the GRF image using multiple thresholds. In the generated GRF image, a threshold-based segmentation is normally carried out to obtain road markings. However, intensity values gradually fade from the scanning center to its two sides. This variation is because intensity values depend on the following: 1) the scanning range from the laser sensor to the target; 2) the incidence angle of the laser beam; and 3) material properties of the target. Accordingly, we propose a point-density-dependent multithreshold segmentation method based on the variations of scanning distance. Within different ranges of the scanning distances, local optimal segmentation thresholds are adaptively estimated.

   We observe that point density approximates normality. Thus, a Gaussian normal distribution can be fitted to obtain two estimated parameters: mean μ and standard deviation σ. Based on the "68–95–99.7" rule of a normal distribution, which says that about 68% of values within one standard deviation σ away from the mean, about 95% of the values within two standard deviations, and about 99.7% within three standard deviations, we assume that intensity variation follows this rule. Thus, according to the three-sigma rule, the corresponding ranges are determined to vertically section data into a number of bins, on each of which we calculate an optimal threshold for segmentation by the method of Otsu [25], which is widely implemented as the default approach to image thresholding.
3) Morphological operations, which refines the extracted road markings by removing noise and filling out holes. With the proposed segmentation method, the extracted road markings still contain noise and are incomplete. By knowing the form and the structure of road markings, a morphological closing operation is defined. Although there are many types of road markings, such as crosswalks, characters, words, symbols, and arrows, most of them are linearly shaped. To simplify convolution, a horizontally linear shaped structuring element is used to dilate and erode the extracted road markings. The linear structure with length l and direction θ is denoted by $K_{\text{line}\,\theta}(l)$. The direction θ is determined by trajectory data. The length $l = 3$ pixels is selected for convoluting road markings.

C. Applications of Road Surface Extraction: Pavement Cracks

Similarly, the method for extracting cracks is proposed based on the interpolated GRF image and mainly includes the following three steps: 1) thresholding, which segments the generated GRF image into a number of crack candidates; 2) crack enhancement, which enhances crack pixels from a noisy and corrupted background by applying iterative tensor voting to the GRF image; and 3) morphological thinning, which extracts the enhanced cracks from the background.

The visual appearance of cracks in the near infrared is usually darker than that in the normal road surface because of the following factors: 1) the increasing surface roughness and

shadows cause reflectance differences between the actual pavement and the high-severity cracks; 2) the concave-shaped cracks make noncracked road pavements brighter; and 3) deeper layers exposed by cracks increase hydrocarbon absorption and highlight the contrary spectral signals with pavement surfaces [41]. Based on intensity values, we first segment a GRF image to obtain possible cracks (crack candidates). After thresholding, we use tensor voting to enhance crack candidates in the GRF images. The tensor voting framework outperforms other methods for identifying cracks because of its capability of preserving all possible sharp curvilinear structures in the presence of a severe noise and providing a very high computational efficiency. In two dimension, a second-order symmetric nonnegative definite tensor is represented by a 2×2 matrix, which is decomposed as [42], [43]

$$T = (\lambda_1 - \lambda_2) e_1 e_1^T + \lambda_2 \left(e_1 e_1^T + e_2 e_2^T \right) \tag{8}$$

where λ_1 and λ_2 $(\lambda_1 > \lambda_2)$ are the eigenvalues. e_1 and e_2 are the corresponding eigenvectors. Geometrically, the tensor is visualized as an ellipse shaped by the tensor eigenvectors' directions and eigenvalues' magnitudes. The first term in (9) is termed as a stick tensor, indicating an elementary curve element with e_1 as its curve normal. The second term is called a ball tensor, indicating a perceptual structure without preferred orientation.

Each crack candidate is initially encoded by a ball tensor with unit saliency, in a form of a 2×2 identity matrix. After the construction of the tensor space, the first round of ball tensor voting is performed using the ball voting field. The ball tensors only cast votes to other ball tensors in their voting fields. We call this tensor voting as sparse ball voting because votes are only cast from tensors to tensors, which means noncracks do not join in this voting.

After large-scale sparse ball voting, all the tensors corresponding to the crack candidates obtain rough orientations and magnitudes. However, the mapped cracks are inaccurate and lack saliency. A round of stick voting is required to refine the orientations and to obtain a saliency map of cracks. Each oriented crack candidate is further encoded as a stick tensor. A dense voting process is then executed with the stick field.

Usually, after the dense stick voting process, curvilinear cracks are enhanced on the resultant saliency map. However, the cracks in the GRF image are presented with much noise and a low contrast with their surroundings. Only one round of dense stick voting could not achieve a good saliency map for the cracks. An iterative scheme is thus proposed to gradually refine the previous results of the dense stick voting, which is termed as iterative tensor voting (ITV). For each iteration, dense stick voting is employed with the stick voting field. As such, each iteration refines the previous one. With the iterative scheme, the tensor with high $\lambda_1 - \lambda_2$ values seems to be concentrated.

To further remove noise and obtain cracks in the crack probability map, a 4-pass-per-iteration morphological thinning algorithm is applied. The algorithm serves to thin the cracks down to their median axes, by peeling off their boundary pixels. After the implementation of the algorithm proposed by Jang and Chin [44], the proposed algorithm produces a converged 8-connected one-pixel-thick skeleton.

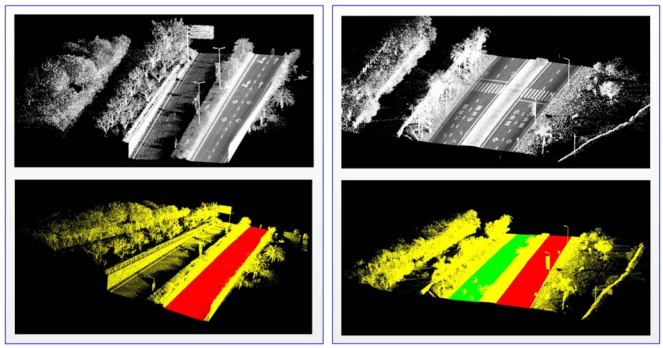

Fig. 4. (Top) Raw MLS data and (bottom) extracted road surfaces. (a) Huandao data set. (b) ICEC data set.

V. Experiments and Discussions

A. Road Surfaces

Six parameters were used for road surface extraction. T_{bs} and T_{pw} are used at the stage of data profiling, T_{cs} and ΔL_j are used at the stage of pseudo scan line generation, and G_i and S_{slope} are used at the stage of curb detection. In our study, according to prior knowledge about road surfaces, we predefined four thresholds, namely, $L_T = 5$ cm, $G_{\min} = 8$ cm, $G_{\max} = 30$ cm, and $S_T = 60^\circ$. As there are no sharp turnings and curves on the roads, we kept $T_{bs} = 3.0$ m, $T_{pw} = 25$ cm, and $T_{cs} = 5$ cm through the following experiments.

We tested our road surface algorithm on two data sets selected from the survey conducted on April 23, 2012: Huandao containing 8.4 million points and ICEC containing 5.4 million points, as shown in Fig. 4. With these thresholds, curbs were extracted from the profiles and fitted into two smooth edges of the road. A visual inspection demonstrates the good extraction results of road surfaces, as shown in Fig. 4. To quantitatively assess the proposed algorithm, we compared the extracted road surfaces with the reference points collected by a smart station Leica TS15i-1/GS15, which provides measurements at the millimeter level. Twenty and fifteen reference points are used for validating the Huandao and IECE data sets, respectively. The Euclidean distances between the positions of the extracted and the references were calculated. A box plot for the accuracy of the extracted road edges is shown in Fig. 5. In each box, the central line represents the median value, whereas its lower and upper edges represent the 25% and 75% percentiles. The minimum and maximum values are represented by the lower and upper adjacent values. A mean and median value close to zero indicates high accuracy. Similarly, we calculated the root-mean-square error (RMSE) values for the two data sets in horizontal and vertical, respectively. The estimated horizontal and vertical RMSEs of the Huandao data set are 8.6 and 2.1 cm, respectively; whereas the ICEC data set has 7.6 and 2.1 cm in horizontal and vertical accuracies, respectively.

To assess computational efficiency, the proposed algorithm was tested on a personal computer with a 3.30-GHz Intel(R) Core(TM) i3-2120 central processing unit. Thus, the running time is about 1.01 and 0.78 s for the Huandao and ICEC data sets, respectively. Although operations in the road surface extraction process are mostly performed on 3-D data, the

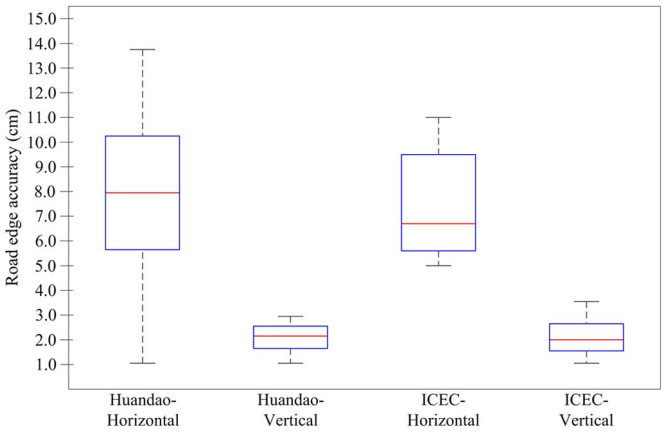

Fig. 5. Box plot for the accuracy of the extracted road edges.

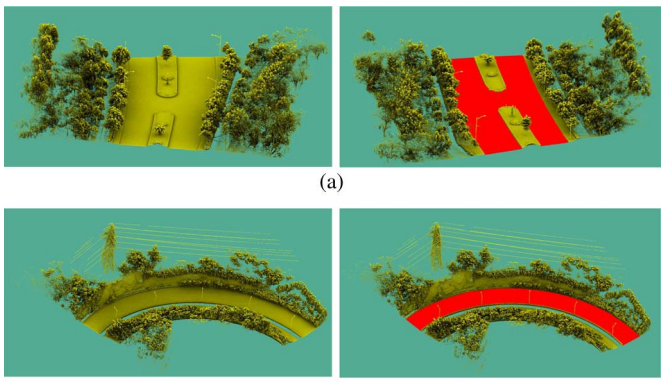

Fig. 6. Two road sections including (left) raw MLS data and the (right) extracted road surfaces. (a) Road 1. (b) Road 2.

process is computationally efficient because of no data indexing structures required for data querying and searching. Thus, our algorithm is a feasible means to detect road surfaces in real time and provides a strong support to inspect road-related features efficiently.

To demonstrate the ability of our algorithm to different road types, we tested it on the two distinct road sections: Road 1 and Road 2, as shown in Fig. 6. Fig. 6(a) shows a road section with green belts containing trees, shrubs, herbaceous perennials, and ornamental grasses. Visual inspection demonstrates that road surface points are completely and accurately extracted, although some points on curbs are misclassified as road surface points at the semicircles of green belts. Based on the assumption that road surface is flat in a small local neighborhood, points close to the extracted road edges were selected and fitted by a RANSAC algorithm to remove misclassified points. Fig. 6(b) shows a road section with a large horizontal curvature. A large T_{bs} could cause a decrease of the extracted curb points on the outer side of the road, leading to a large fitting error and, thus, inaccurate road edge extraction. Thus, we reduced the value of T_{bs} from 3.0 to 1.0 m to obtain more road sections and road profiles and, finally, to detect more curb points for accurately extracting road edges. The trajectory data determine the selection of T_{bs}. The extracted road surface points indicate that our algorithm is able to handle roads with curvatures.

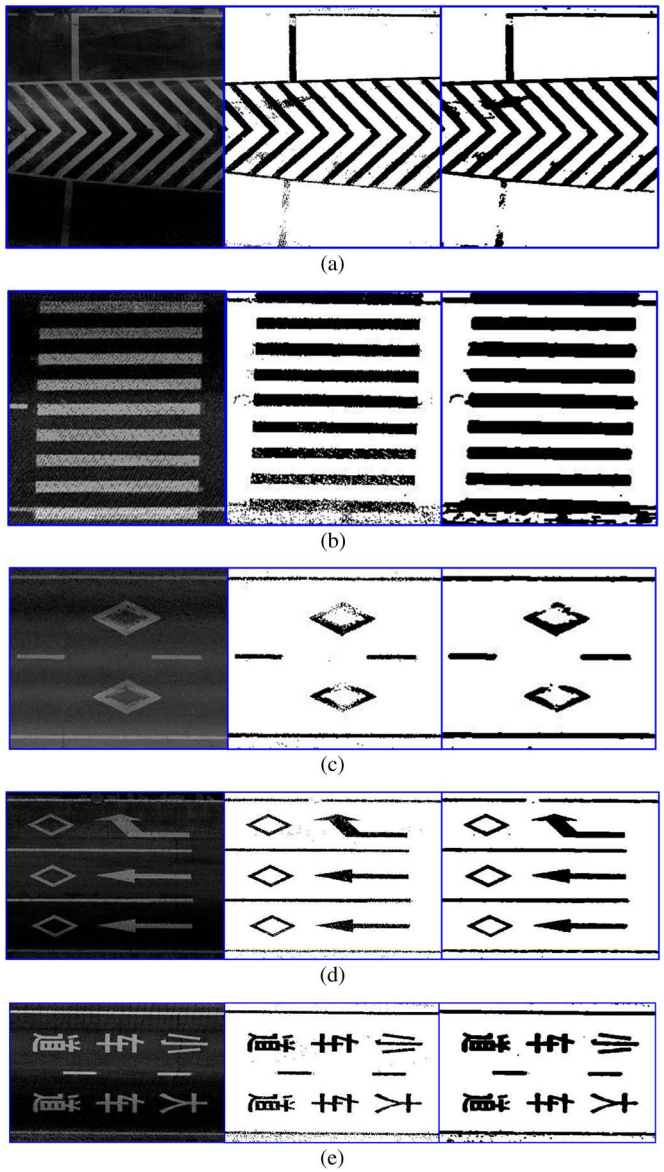

Fig. 7. Proposed algorithm tested on five road sections with different types of road markings: (left) GRF image; (middle) point-density-dependent multithresholding segmentation results; (right) extracted road markings. (a) Marking 1 (hatch and solid line markings). (b) Marking 2 (crosswalk markings). (c) Marking 3 (symbol and continuous and broken lane markings). (d) Marking 4 (arrow, symbol, and continuous and broken lane markings). (e) Marking 5 (word and continuous and broken lane markings).

B. Road Markings

The applicability of the proposed road marking extraction algorithm was tested on five road sections containing several types of road markings, such as arrow, symbol, lane, word, and hatch markings. To the best of our knowledge, currently, there is no data set designed for evaluating the performance of road marking extraction methods from MLS data.

We kept $T_{cs} = 4$ cm for generating GRF images. Fig. 7 shows that all road markings are correctly and completely identified. By comparing the extracted road markings with the manually interpreted ground truth, we quantitatively evaluate the extracted road markings using the following three measures: completeness (cpt), correctness (crt), and F-*measure*. cpt describes how complete the extracted road markings are, whereas

TABLE IV
QUANTITATIVE ASSESSMENT OF THE PROPOSED ALGORITHM ON FIVE ROAD SECTIONS

Measures	Marking 1	Marking 2	Marking 3	Marking 4	Marking 5
cpt	0.94	0.92	0.88	0.96	0.97
crt	0.91	0.89	0.87	0.93	0.84
F-measure	0.93	0.90	0.88	0.95	0.90

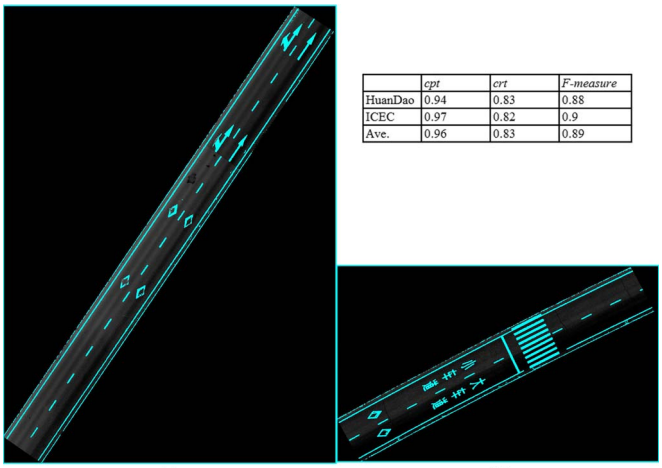

Fig. 8. Extracted road markings overlaid on the GRF images. (a) Huandao data set. (b) ICEC data set.

crt indicates what percentage of the extracted road markings are valid. cpt is expressed as $\text{cpt} = C_p/Rf$, and crt is defined as $\text{crt} = C_p/E_p$, where C_p denotes the number of pixels belonging to the real road markings, Rf is the number of the ground truth pixels collected by the manual interpretation method, and E_p represents the number of pixels extracted by the proposed algorithm. *F-measure* is an overall score, which is defined as $F = 2 \times ((\text{cpt} \cdot \text{crt})/(\text{cpt} + \text{crt}))$.

Table IV shows that the crt values are greater than 0.82, the cpt values are higher than 0.92, and the *F-measure* values range from 0.87 to 0.96. The three measures, i.e., cpt, crt, and *F-measure*, for all cases, indicate that the proposed method is robust to different types of road markings.

We conducted tests on the Huandao and ICEC data sets, respectively. The road markings extracted from the data sets are displayed in Fig. 8. We overlaid the extracted road markings on the GRF image. The close-up views of two data sets show that our algorithm completely extracts road markings with less noise. The quantitative analysis shows that, for all the road markings, the values of cpt, crt, and *F-measure* are consistently above 0.94, 0.82, and 0.88, respectively.

The experimental results demonstrate that our algorithm is able to extract road markings from a large amount of MLS data because of the following: 1) the extracted road surface serves prior knowledge to facilitate the road marking extraction process and improve the correctness of road markings; 2) a combination of local and global intensity weights contributes to the generation of GRF image; and 3) the proposed point-density-dependent multithreshold segmentation method overcomes inconsistent intensity values caused by the incidence angle of laser pulses and the range of the scanner center to the illuminated road surface.

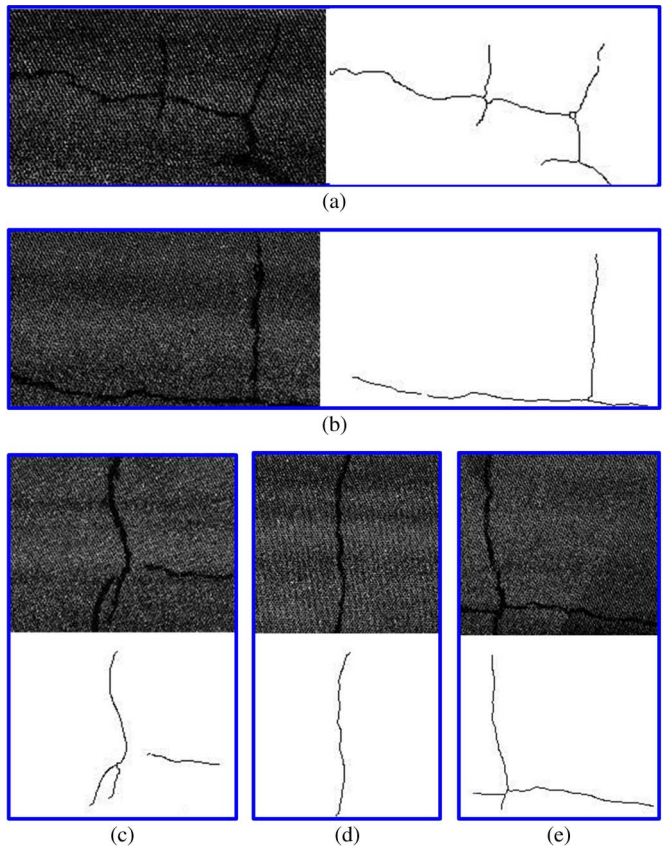

Fig. 9. GRF images and extracted cracks. (a) Crack 1. (b) Crack 2. (c) Crack 3. (d) Crack 4. (e) Crack 5.

TABLE V
QUANTITATIVE ASSESSMENT OF THE PROPOSED ALGORITHM ON FIVE CRACKS

Measures	Crack 1	Crack 2	Crack 3	Crack 4	Crack 5
cpt	0.96	0.96	0.98	0.98	0.96
crt	0.85	0.88	0.89	0.92	0.90
F-Measure	0.90	0.92	0.93	0.95	0.93

C. Pavement Cracks

From the Huandao and ICEC data sets, we selected an area of interest containing small cracks with a few centimeters in width extending to large alligator cracks up to the size of 10 cm. Our main focus was to accurately extract these cracks in the GRF image. Fig. 9 shows Cracks 1–5 selected from the GRF image with a ground sample distance of 2 cm. Cracks 3–5 have a size of 200 × 200 pixels, and Cracks 1 and 2 have a size of 250 × 150 pixels. These cracks contain low signal-to-noise ratio (SNR) rates and low contrasts with their surroundings in the GRF images. With our proposed algorithm, curvilinear cracks were enhanced, and their surrounding noise was suppressed or removed. Visual inspection shows that cracks are well extracted, consistent with the original GRF images, as shown in Fig. 9. From a quantitative perspective, we assessed the extracted cracks using cpt, crt, and *F-measure*. Table V lists three measures for five cracks. We achieved the cpt values higher than 0.96, the crt values greater than 0.85, and the *F-measure* values higher than 0.90, indicating that the proposed

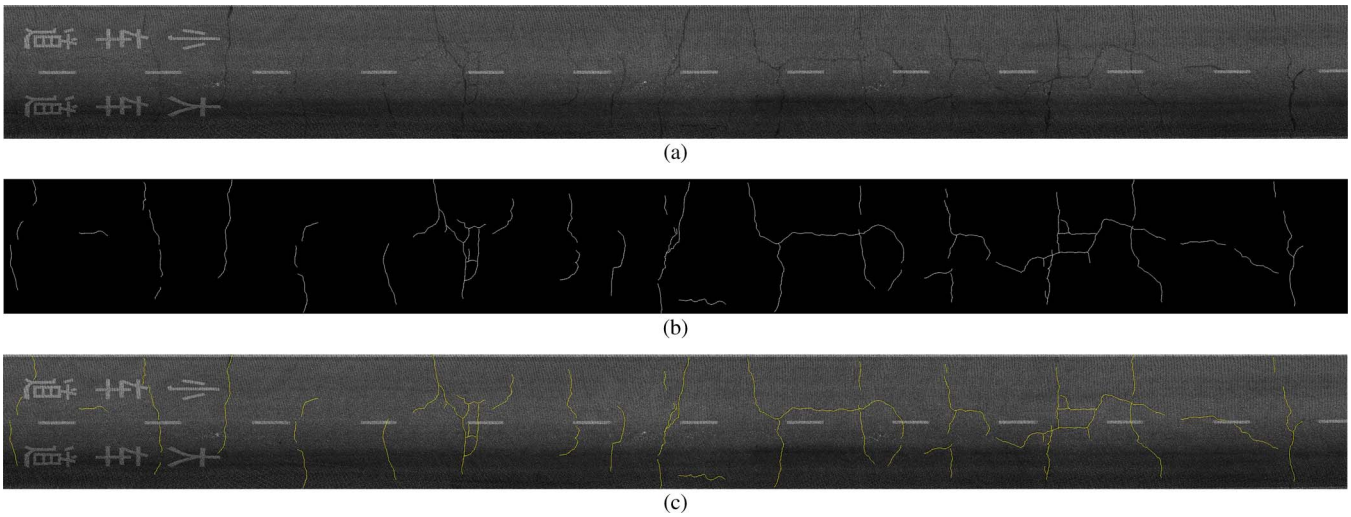

Fig. 10. Crack detection results for the 75-m-long road section. (a) GRF image. (b) Detected cracks. (c) Detected cracks overlaid on the GRF image.

algorithm is robust to different types of cracks presented in the noisy and corrupted GRF images.

To further demonstrate the performance of the proposed algorithm, we selected a road section covering a number of cracks, as shown in Fig. 10. The selected two-lane road section has a length of 75.4 m and a width of around 8 m [see Fig. 10(a)]. The number of road points is 2 547 020. The resolution of GRF images is 2 cm, which means that the width of cracks shown in the GRF image is larger than 2 cm, indicating these cracks are desperately needed to be repaired, such as sealing or filling operations. Fig. 10(b) and (c) shows extracted cracks and their overlaid results in the GRF image. As shown in Fig. 10(c), we extracted almost all cracks with widths over 2 cm. In order to accelerate the detection procedure, the 75-m-long road was segmented into a series of small images with a size of 200 $\times$ 125 pixels. The total processing time for all small images is approximately 5995 s, computationally intensive due to iteration operations involved in the tensor voting process. However, it could be solved in the recent research of distribution computation because the voting process of each tensor is independent. In a parallel environment, with a multithread scheme, computation burdens can be distributed on each parallel procedure, indicating that computational performance will be obviously improved and that time complexity will be greatly reduced. In addition, although the resolution of current MLS data limits us to detect cracks over 2 cm, hardware advancement in the foreseeable future will allow us to detect cracks at millimeter level.

VI. Conclusion

We have presented a RIEGL VMX-450 system used for transportation-related applications, indicating that MLS technology is suitable for collecting 3-D geospatial data of road networks and corridor environments and conducting road inventory and transportation-related surveying.

Assuming that curbs are road boundaries, we have proposed a curb-based road surface extraction algorithm to extract road surface points from large volumes of MLS data. Our algorithm consists of four steps: data profiling, pseudo scan line generation, curb detection, and road edge interpolation. The experimental results demonstrated that the accuracies of detected road surfaces meet the requirements of transportation-related road applications, such as mapping natural terrain, assessing roadway condition, conducting Geographic Information System, and modeling urban traffic. Based on the detected road surface data, we have presented automated road marking and pavement crack extraction algorithms, respectively. Our road marking extraction algorithm achieved stable performance on six road sections, which include arrow, solid, symbol, crosswalk, words, and hatch markings. Different from highly retroreflective road markings, cracks are represented by nonuniform intensity, the low contrast with their surroundings, and low SNR owing to particle materials of asphalt-concrete-surfaced roads. Our algorithm used ITV to successfully enhance curvilinear crack structures from noisy and corrupted road data.

Our research on MLS data provides valuable insights into and a prototype of road feature extraction at all levels of transportation agencies and opens a window to advanced MLS technologies for road surveying.

References

[1] V. Tao and J. Li, *Advances in Mobile Mapping Technology*. London, U.K.: Taylor & Francis, 2007.

[2] "A new tool for engineering surveys Mobile Terrestrial LiDAR Scanning (MTLS)," *Ontario's Transp. Technol. Transf. Dig. Ministry Transp.*, vol. 19, no. 1, p. 3, 2013, Road Talk.

[3] N. Haala, M. Peter, A. Cefalu, and J. Kremer, "Mobile Lidar mapping for urban data capture," in *Proc. 14th Int. Conf. Virtual Syst. Multimedia*, 2008, pp. 95–100.

[4] V. Ussyshkin, "Mobile laser scanning technology for surveying application: From data collection to end-products," in *Proc. FIG Working Week*, Eilat, Israel, May 3–8, 2009, pp. 1–13.

[5] D. Stauth and M. Olsen, "Mobile LIDAR technology expanding rapidly," Data accessed: Aug. 23, 2013. [Online]. Available: http://oregonstate.edu/ua/ncs/archives/2013/mar/mobile-lidar-technology-expanding-rapidly

[6] H. Lee, "Standardization of distress measurements for the network-level pavement management system, pavement management implementation," in *ASTM STP 1121*, F. B. Holt and W. L. Gramling, Eds. Philadelphia, PA, USA: American Society for Testing and Materials, 1992, pp. 424–436.

[7] Y. Tsai, V. Kaul, and R. M. Mersereau, "Critical assessment of pavement distress segmentation methods," *J. Transp. Eng.*, vol. 136, no. 1, pp. 11–19, Jan. 2010.

[8] B. Carnaby, "Poor road markings contribute to crash rates," in *Proc. Australasian Road Safety Res. Policing Educ. Conf.*, Wellington, New Zealand, Nov. 14–16, 2005, pp. 1–10, [CD-ROM], (CD401).
[9] G. Jacobs, "Uses in transportation," High-Definition Surveying: 3D Laser Scanning. Professional Surveyor Magazine, Apr. 2005.
[10] C. K. Toth, "R&D of mobile lidar mapping and future trends," in *Proc. ASPRS Annu. Conf.*, Baltimore, MD, USA, Mar. 9–13, 2009, pp. 1–7.
[11] S. Pu, M. Rutzinger, G. Vosselman, and S. O. Elberink, "Recognizing basic structure from mobile laser scanning data for road inventory studies," *ISPRS J. Photogramm. Remote Sens.*, vol. 66, no. 6, pp. s28–s39, Dec. 2011.
[12] O. Takashi and T. Kiyokazu, "Lane recognition using on-vehicle lidar," in *Proc. IEEE Intell. Veh. Symp.*, Tokyo, Japan, Jun. 13–15, 2006, pp. 540–545.
[13] L. Smadja, J. Ninot, and T. Gavrilovic, "Road extraction and environment interpretation from Lidar sensors," *ISPRS Achieves*, vol. 38, no. 3A, pp. 281–286, Sep. 2010.
[14] X. Yuan, C. Zhao, and H. Zhang, "Road detection and corner extraction using high definition Lidar," *Inf. Technol. J.*, vol. 9, no. 5, pp. 1022–1030, Sep. 2010.
[15] D. Manandhar and R. Shibasaki, "Vehicle-borne Laser Mapping System (VLMS) for 3-D GIS," in *Proc. IEEE IGARSS*, 2001, vol. 5, pp. 2073–2075.
[16] B. J. Li, Q. Q. Li, W. Z. Shi, and F. F. Wu, "Feature extraction and modeling of urban building from vehicle-borne laser scanning data," in *Proc. Int. ISPRS Archives*, 2004, pp. 934–940.
[17] X. Chen, M. Stroila, and R. Wang, "Next generation map marking: Geo-referenced ground-level LiDAR point clouds for automatic retro-reflective road feature extraction," in *Proc. 17th ACM SIGSPATIAL Int. Conf. Adv. GIS*, Seattle, WA, USA, Nov. 4–6, 2009, pp. 488–491.
[18] Z. Liu, J. Wang, and D. Liu, "A new curb detection method for unmanned ground vehicles using 2D sequential laser data," *Sensors*, vol. 13, no. 1, pp. 1102–1120, Jan. 2013.
[19] L. Zhou and G. Vosselman, "Mapping curbstones in airborne and mobile laser scanning data," *Int. J. Appl. Earth Observ. Geoinf.*, vol. 18, pp. 293–304, Aug. 2012.
[20] W. Zhang, "LiDAR-based road and road-edge detection," in *Proc. IEEE Intell. Veh. Symp.*, San Diego, CA, USA, Jun. 2010, pp. 845–848.
[21] S. Yu, S. R. Sukumar, A. F. Koschan, D. L. Page, and M. A. Abidi, "3D reconstruction of road surfaces using an integrated multi-sensory approach," *Opt. Lasers Eng.*, vol. 45, no. 7, pp. 808–818, Jul. 2007.
[22] A. Boyko and T. Funkhouser, "Extracting roads from dense point clouds in large scale urban environment," *ISPRS J. Photogramm. Remote Sens.*, vol. 66, no. 6, pp. S2–S12, Dec. 2011.
[23] Q. Li, Q. Zou, D. Zhang, and Q. Mao, "FoSA: F* seed-growing approach for crack-line detection from pavement images," *Image Vis. Comput.*, vol. 29, no. 12, pp. 861–872, Nov. 2011.
[24] H. N. Koutsopoulos, I. El Sanhouri, and A. B. Downey, "Analysis of segmentation algorithms for pavement distress images," *J. Transp. Eng.*, vol. 119, no. 6, pp. 868–888, Dec. 1993.
[25] N. Otsu, "A threshold selection method from gray-level histogram," *IEEE Trans. Syst., Man, Cybern.*, vol. SMC-9, no. 1, pp. 62–66, Jan. 1979.
[26] A. Cuhadar, K. Shalaby, and S. Tasdoken, "Automatic segmentation of pavement condition data using wavelet transform," in *Proc. IEEE Can. Conf. Elect. Comput. Eng.*, 2002, vol. 2, pp. 1009–1014.
[27] N. Tanaka, "A crack detection method in road surface image using morphology," in *Proc. MVA IAPR Conf.*, Makuhari, Japan, Nov. 17–19, 1998, pp. 154–157.
[28] M. Gavilán, D. Balcones, O. Marcos, D. F. Llorca, and M. A. Sotelo, "Adaptive road crack detection system by pavement classification," *Sensors*, vol. 11, no. 10, pp. 9628–9657, Oct. 2011.
[29] T. Saar and O. Talvik, "Automatic asphalt pavement crack detection and classification using neural networks," in *Proc. 12th Biennial Baltic Electron. Conf.*, Tallinn, Estonia, Oct. 4–6, 2010, pp. 345–348.
[30] P. Charbonnier, F. Diebolt, Y. Guillard, and F. Peyret, "Road markings recognition using image processing," in *Proc. IEEE Conf. Intell. Transp. Syst.*, Boston, MA, USA, Nov. 1997, pp. 912–917.
[31] J. Rebut, A. Bensrhair, and G. Toulminet, "Image segmentation and pattern recognition for road marking analysis," in *Proc. IEEE Int. Symp. Ind. Electron.*, May 2004, vol. 1, pp. 727–732.
[32] J. C. McCall and M. M. Trivedi, "Video based lane estimation and tracking for driver assistance: Survey, system, and evaluation," *IEEE Trans. Intell. Transp. Syst.*, vol. 7, no. 1, pp. 20–37, Mar. 2006.
[33] A. Kheyrollahi and T. P. Breckon, "Automatic real-time road marking recognition using a feature approach," *Mach. Vis. Appl.*, vol. 23, no. 1, pp. 123–133, Jan. 2010.
[34] R. Danescu and S. Nedevschi, "Detection and classification of painted road objects for intersection assistance applications," in *Proc. IEEE Conf. Intell. Transp. Syst.*, Funchal, Portugal, Sep. 19–22, 2010, pp. 433–438.
[35] B. Yang, L. Fang, Q. Li, and J. Li, "Automated extraction of road markings from mobile Lidar point clouds," *Photogramm. Eng. Remote Sens.*, vol. 78, no. 4, pp. 331–338, Apr. 2012.
[36] A. Jaakkola, J. Hyyppä, H. Hyyppä, and A. Kukko, "Retrieval algorithms for road surface modeling using laser-based mobile mapping," *Sensors*, vol. 8, no. 9, pp. 5238–5249, Sep. 2008.
[37] G. Vosselman, "Advanced point cloud processing," in *Proc. Photogramm. Week*, Heidelberg, Germany, 2009, pp. 137–146.
[38] C. Glennie, "Rigorous 3D error analysis of kinematic scanning LIDAR systems," *J. Appl. Geod.*, vol. 1, no. 3, pp. 147–157, Nov. 2007.
[39] P. Rieger, N. Studnicka, M. Pfennigbauer, and G. Zach, "Boresight alignment method for mobile laser scanning systems," *J. Appl. Geod.*, vol. 4, no. 1, pp. 13–21, Jan. 2010.
[40] S. Lim *et al.*, "Accuracy assessment of a mobile terrestrial lidar survey at Padre Island National Seashore," *Int. J. Remote Sens.*, vol. 34, no. 18, pp. 6355–6366, Sep. 2013.
[41] H. Martin, "Spectral characteristics of asphalt road surfaces," in *Remote Sensing of Impervious Surfaces*, Q. Weng, Ed. New York, NY, USA: Taylor & Francis, 2008, pp. 237–247.
[42] G. Medioni, M. S. Lee, and C.-K. Tang, *A Computational Framework for Segmentation and Grouping*. Amsterdam, The Netherlands: Elsevier, 2000.
[43] L. A. Loss, G. Bebis, and B. Parvin, "Iterative tensor voting for perceptual grouping of ill-defined curvilinear structures," *IEEE Trans. Medical Imaging*, vol. 30, no. 8, pp. 1503–1513, Aug. 2011.
[44] B. K. Jang and R. T. Chin, "Analysis of thinning algorithms using mathematical morphology," *IEEE Trans. Pattern Anal. Mach. Intell.*, vol. 12, no. 6, pp. 541–551, Jun. 1990.

Haiyan Guan received the Ph.D. degree in geomatics from University of Waterloo, Waterloo, ON, Canada, in 2014.

She is a Senior Research Fellow with the Department of Geography and Environmental Management, University of Waterloo. She has coauthored over 30 research papers published in refereed journals, books, and proceedings. Her research interests include airborne, terrestrial, and mobile laser scanning data processing algorithms and 3-D spatial modeling and reconstruction of critical infrastructure and landscape.

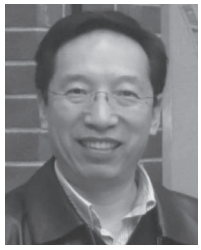

Jonathan Li (M'00–SM'11) received the Ph.D. degree in geomatics engineering from University of Cape Town, Cape Town, South Africa.

He is with the Ministry of Education Key Laboratory of Underwater Acoustic Communication and Marine Information Technology and the School of Information Science and Engineering, Xiamen University, Xiamen, China. He also heads the Waterloo Laboratory for GeoSpatial Technology and Remote Sensing, Faculty of Environment, University of Waterloo, Waterloo, ON, Canada, where he is a Professor and an elected member of the University Senate. He has coauthored over 200 publications, over 60 of which were published in refereed journals. His research interests include information extraction from Earth observation images and 3-D surface reconstruction from mobile LiDAR point clouds.

Dr. Li is the Chair of the intercommission working group I/VA on Mobile Scanning and Imaging Systems of the International Society for Photogrammetry and Remote Sensing (2012–2016), the Vice Chair of the Commission on Hydrography of the International Federation of Surveyors (2011–2014), and the Vice Chair of the Commission on Mapping from Remote Sensor Imagery of the International Cartographic Association (2011–2015).

Yongtao Yu received the B.S. degree in computer science from Xiamen University, Xiamen, China, in 2010. He is currently working toward the Ph.D. degree in the Department of Computer Science, Xiamen University.

His research interests include computer vision, machine learning, mobile laser scanning, and point cloud processing.

Michael Chapman received the Ph.D. degree in photogrammetry from Laval University, Quebec, QC, Canada.

He is a Professor of geomatics with the Department of Civil Engineering, Ryerson University, Toronto, ON, Canada. Prior to joining Ryerson University he was a Professor with the Department of Geomatics Engineering, University of Calgary, for 18 years. He has authored or coauthored over 160 technical articles. His research interests include algorithms and processing methodologies for airborne sensors using Global Positioning System/Inertial Navigation System, geometric processing of digital imagery in industrial environments, terrestrial imaging systems for transportation infrastructure mapping, and algorithms and processing strategies for biometrology applications.

Cheng Wang (M'12) received the Ph.D. degree in information and communication engineering from National University of Defense Technology, Changsha, China, in 2002.

He is a Professor and the Associate Dean of the School of Information Science and Technology, Xiamen University, Xiamen, China. He has authored over 80 papers. His research interests include remote sensing image processing, mobile LiDAR data analysis, and multisensor fusion.

Dr. Wang is a Cochair of the working group I/3 of the International Society for Photogrammetry and Remote Sensing, a Council Member of the Chinese Society of Image and Graphics, and a member of The International Society for Optics and Photonics and the IEEE Geoscience and Remote Sensing Society.